


Laboratory precision measurements of optical emissions from coronal ironH. Bekker,^{*} C. Hensel, A. Daniel, A. Windberger, T. Pfeifer, and J. R. Crespo López-Urrutia[†]
Max-Planck-Institut für Kernphysik, Saupfercheckweg 1, 69117 Heidelberg, Germany (Received 26 March 2018; revised manuscript received 5 June 2018; published 19 December 2018)

Total solar eclipses, as the recent one seen across North America, are rare opportunities for optical spectroscopy of the corona. In view of the dearth of accurate rest-frame wavelength data, we measured 11 of the strongest optical coronal lines belonging to Fe X–XIV thereby proving the existence of the Fe XII line at 290.385(8) nm. Four lines, such as the green coronal line at 530.28113(13) nm, were measured with unprecedented precision, allowing in principle for absolute velocity determinations of plasmas with uncertainties of 0.08 km s⁻¹. These results furthermore stringently benchmark the theory of complex open-3*p*-shell ions.

DOI: [10.1103/PhysRevA.98.062514](https://doi.org/10.1103/PhysRevA.98.062514)

The rare few minutes of clear, unobscured observation of the solar atmosphere that total eclipses offer have historically been major opportunities for spectroscopic studies. The earliest such study by Harkness and Young in 1869 led to the discovery of the green coronal line at approximately 530.3 nm [1]. Together with the red coronal line at approximately 637.4 nm and other emission lines, it was correctly attributed to highly charged iron ions around the early 1940s by Grotrian and Edlén [2,3]. Alfvén concluded that the corona has a temperature on the order of 1 MK [4], a surprising result considering that the underlying photosphere has a temperature of maximally only 6000 K. To solve this so-called coronal heating problem, measurements of the optical emission from the corona remain essential to better determine its temperature, composition, magnetic properties, and structure [5–11]. As with previous eclipses, the recent August 21st 2017 one is sure to have yielded a treasure of new data [12,13]. Optical lines of highly charged iron also continue to be observed in many other astronomical objects, for example in red dwarfs [14,15], Seyfert galaxies [16], suspected tidal disruption of a star by a supermassive black hole [17,18], and in supernova remnants [19].

Recently published results obtained with high resolving power spectrographs developed for coronal observations demonstrate the necessity of precise knowledge of the rest-frame wavelengths to interpret velocity-induced Doppler shifts [11]. The open 3*p* shells of the here investigated ions render atomic theory calculations cumbersome as the complex electronic correlations are difficult to reproduce accurately. Moreover, quantum electrodynamics (QED) effects are known to play a significant role in highly charged ions (HCIs), and therefore need to be taken into account as well. Nonetheless, impressive progress has been made in recent years, predictions typically agree at the level of 0.1% with experimentally obtained values [20–24]. However, this still limits the precision of absolute velocity analysis by Doppler shifts of the order of 100 km s⁻¹. Considering that the velocities of stellar

winds are of the same order, the uncertainties on calculations impede analysis employing this method. Additionally, there is increased interest in optical transitions in HCIs from the metrology community, e.g., [25–27]. Their insensitivity to external perturbations and enhanced sensitivity to QED and relativistic effects make them suitable for a wide range of applications such as searches for variation of fundamental constants [28]. The envisioned precision laser spectroscopy experiments rely on a more precise knowledge of transition wavelengths than state-of-the-art atomic theory can deliver [29,30]. Hence, laboratory measurements are crucial for these experiments and for benchmarking atomic theory of systems with complex correlations between electrons in an open shell.

Considering highly charged iron ions, only the wavelengths of the red Fe X and green Fe XIV coronal lines are currently known at the parts-per-million (ppm) level from laboratory measurements [24,31]. Other experimental values are often obtained from observations of the corona so that their precision is inherently limited due to unknown Doppler shifts [32,33]. In this work we employed electron beam ion traps (EBITs) to produce the HCI of interest and grating spectrometers to obtain their spectra with a much improved precision. In an EBIT, the magnetically focused electron beam sequentially ionizes particles in the trapping region by impact [34,35]. The highest obtainable charge state is limited by the electron beam energy E_e , which is determined by the electron beam acceleration potential U_{acc} . This leads to a narrow charge state distribution of the trapped HCI. The trapping potential is mainly determined by the negative space charge of the electron beam. Furthermore, a potential applied on drift tubes prevents the HCIs from escaping in the axial direction. Iron atoms were continuously loaded as a molecular beam of Fe(CO)₅, which is easily disassociated by the electron beam. By applying a shallow enough axial trapping potential, the lighter carbon and oxygen ions were expelled from the trap, thereby evaporatively cooling the remaining iron ions. To ensure a contaminant free ion sample, the trapping potential was inverted every few minutes.

During the first part of this work, overview spectra of Fe X–XIV were obtained in the range from 240–670 nm by

^{*}bekker@mpi-hd.mpg.de[†]crespojr@mpi-hd.mpg.de

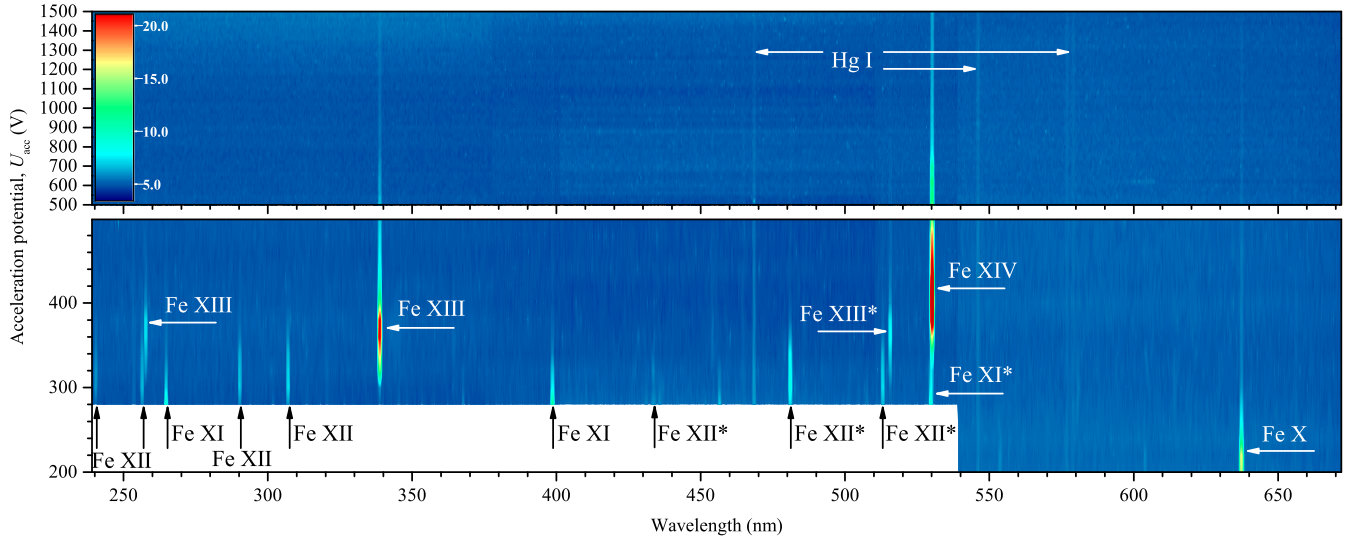


FIG. 1. Spectral map of highly charged iron ions obtained by interpolating spectra obtained at 20 V intervals of U_{acc} , and at several grating angles. To make weak signals more discernible, the color map is scaled with the square root of the intensity (in arbitrary units). Line identifications are indicated where possible, those marked with an asterisk are due to second order diffraction of the grating.

employing a Czerny-Turner type spectrometer of the model Horiba Triax 550 mounted at the FLASH-EBIT [35]. At a fixed angle of the 300 lines mm^{-1} grating, a spectral range of approximately 160 nm could be recorded. Hence, three settings were required to cover the desired range. At each, a sequence of 30-min-long acquisitions was made between which U_{acc} was increased by 20 V up to 1500 V. The region up to 540 nm was acquired at an electron beam current of 30 mA with which stable operation was possible from $U_{\text{acc}} = 290$ V upward. For the part above 540 nm, a current of 20 mA was set, enabling lower values for U_{acc} so that the 638 nm Fe X line could also be observed. The resulting overview is shown in Fig. 1. The color scale was not adjusted to take into account the wavelength dependent efficiency of the setup and the difference in electron beam currents. Hence, not all lines appear clearly in second order. The observed appearance and disappearance of lines with varying U_{acc} was attributed to the production of different iron charge states. As reference for the charge state assignments, the well known and strong Fe XIV line near 530 nm was used. Lines that appeared at consecutively lower (higher) values of U_{acc} belong to corresponding lower (higher) charge states. Several lines that did not show a dependence on U_{acc} could be attributed to Hg emission from overhead fluorescent lamps in the experimental hall. For these exploratory measurements, the entrance slit width was set to 200 μm for an increased photon yield at the cost of reduced resolving power and accuracy.

Gaussians were fitted to the lines to determine their wavelengths; the results are listed in Table I. Successive measurements of the lines at approximately 290, 339, 399, and 530 nm were made using a 2400 lines mm^{-1} grating and a narrower slit width of 70 μm resulting in an instrumental resolving power at 530 nm of $r_{530} = 16 \times 10^3$. Previous observations and identifications of most lines could be found in literature [2,3,32,33]. However, the Fe XII line at 290.385(8) nm was only known from theoretical energy levels and the Ritz value from the NIST atomic spectra database [21,36,37].

For the second part of this work, the four relatively strong lines at approximately 637, 789, 339, and 530 nm were measured at the Heidelberg EBIT (HD-EBIT) with a McPherson Model 2062 spectrometer [34]. The 2000 mm focal length of this device gives a much improved linear dispersion as compared to the Triax, which has a focal length of only 550 mm. It was operated with an 1800 lines mm^{-1} grating, or in the case of the 339 nm line, a 3600 lines mm^{-1} grating. The resolving power was further increased by setting the entrance slit width such that the linewidths were dominated by Doppler broadening. This in turn was reduced by decreasing the trap depth to enhance evaporative cooling and by running the EBIT at relatively low currents of maximally 20 mA. These measures decreased the number of trapped ions, so exposures

TABLE I. Wavelengths in air λ of the Fe lines, as measured at the FLASH-EBIT. Literature references to the identifications are given in the first column. Some lines (indicated by *) were observed in the first and second grating diffraction order, whereas the line at 216 nm was seen only in the second order. Wavelengths obtained using the 2400 lines mm^{-1} grating are indicated with a †.

Ion	Transition	λ (nm)
Fe XII [32]	$[\text{Ne}]3s^23p^3(^2D_{5/2} - ^4S_{3/2})$	216.86(6)*
Fe XII [32]	$[\text{Ne}]3s^23p^3(^2D_{3/2} - ^4S_{3/2})$	240.55(4)*
Fe XII [32]	$[\text{Ne}]3s^23p^3(^2P_{3/2} - ^2D_{3/2})$	256.60(4)*
Fe XIII [32]	$[\text{Ne}]3s^23p^2(^1D_2 - ^3P_1)$	257.87(4)*
Fe XI [32]	$[\text{Ne}]3s^23p^4(^1D_2 - ^3P_2)$	264.89(4)*
Fe XII [21,36,37]	$[\text{Ne}]3s^23p^3(^2P_{3/2} - ^5D_{5/2})$	290.385(8)†
Fe XII [33]	$[\text{Ne}]3s^23p^3(^2P_{1/2} - ^2D_{3/2})$	307.17(6)
Fe XIII [33]	$[\text{Ne}]3s^23p^2(^1D_2 - ^3P_2)$	338.788(6)†
Fe XI [33]	$[\text{Ne}]3s^23p^4(^1D_2 - ^3P_1)$	398.683(8)†
Fe XIV [3]	$[\text{Ne}]3s^23p^1(^2P_{3/2} - ^2P_{1/2})$	530.276(6)†
Fe X [2]	$[\text{Ne}]3s^23p^5(^2P_{1/2} - ^2P_{3/2})$	637.41(6)

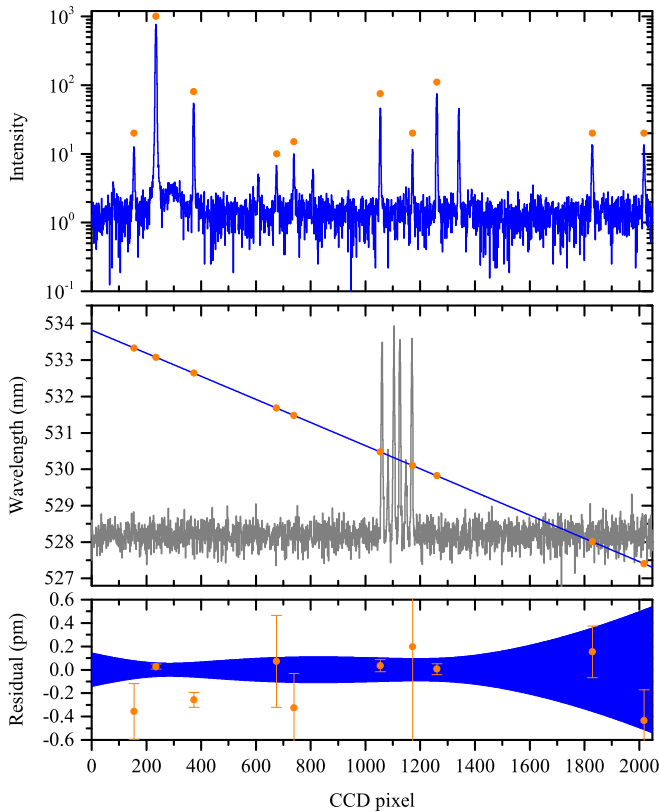


FIG. 2. Top: Calibration spectrum of the Pt-Ne hollow cathode lamp. The lines used for the calibration are indicated with orange circles. Here $r_{530} = 40 \times 10^3$. Middle: The pixel positions of the calibration lines are plotted against their known wavelengths [37,38]. A parabola (blue) is fitted to the data to obtain the calibration function. Higher order polynomials did not improve the quality of the fit, nor did the resulting calibration function change the end result for the wavelength determination. In gray, a single 30 min acquisition of the Fe^{13+} spectrum is shown to indicate the position of the Zeeman split 530 nm line relative to the calibration lines. Bottom: Fit residuals, and the $1\text{-}\sigma$ confidence band.

of 10 to 20 h were needed. During this time, the camera was read out every 30 min, allowing for an intermediate calibration spectrum to be recorded. A typical one, and the resulting calibration function for the Fe^{13+} measurement, are shown in Fig. 2. For each Fe measurement either a Pt-Ne or Fe-Ar hollow cathode lamp was selected depending on its spectral richness in the observed range [38–46]. Its light homogeneously illuminated a slit at an intermediate real image of the trapped ions using a movable diffuse reflector. As tests confirm, on a range larger than the extent of the trapped ion cloud its position does not influence the calibration. Each 30 min Fe acquisition was calibrated with the average of its pre- and post-acquisition calibration functions to reduce the effect of slow mechanical drifts of the grating (which were already small in our laboratory due to temperature stabilization the level of ± 0.25 K) to a negligible level. Background spectra were measured and subtracted, and pixels affected by cosmic ray events were excluded from further analysis. The acquisitions thus processed were combined to obtain the cumulative spectra of Fig. 3. The uncertainties on the data

comprise the thermal and read-out noise of the camera as well as shot noise.

Due to the magnetic field strength of $B = 8.000(5)$ T at the trap center, the Zeeman effect causes the observed lines to be split into several components. The resulting line shapes were fitted with a Zeeman model line-shape function that proved to be suitable in previous work [29],

$$f(E) = \sum_{\Delta m_J} a_{\Delta m_J} \sum_{m_J} \langle J, m_J, 1, \Delta m_J | J', m'_J \rangle^2 \times \exp\left(\frac{\{E - E_0 - \mu_B B [m_J(g - g') + \Delta m_J g']\}^2}{2w^2}\right).$$

This takes into account: the central transition energy E_0 ; total angular momentum quantum numbers of the upper J and lower J' levels; the g_J factors of the upper g and lower levels g' ; the upper level magnetic quantum number m_J , and the change of it $\Delta m_J = -1, 0, 1$; relative amplitudes within one Δm_J group as determined by the squared Clebsch-Gordan coefficients $\langle J, m_J, 1, \Delta m_J | J', m'_J \rangle^2$; the amplitudes for the different polarizations $a_{-1} = a_1, a_0$; the common linewidth w of the individual components; and finally, the Bohr magneton μ_B . In this model it is assumed that all magnetic sublevels are equally populated. Even so, $a_{\Delta m}$ are required to take into account the difference in efficiency for the polarizations parallel and perpendicular to the spectrometer grating, which is known only approximately. Our Zeeman model does not take into account second-order shifts, which are typically a factor of 10^4 smaller than the first-order shifts. This was confirmed for the transitions investigated here with the flexible atomic code [47]. Hyperfine structure was also beyond detection due to the small overlap of the $3p$ orbitals with the nucleus and the mostly spinless nuclei of iron. The isotope shift is minimal since at 92% abundance the isotope iron-56 makes up the vast majority of the sample. All wavelengths in this work are given in air; for the fit these were converted to energy units employing the empirical equation determined by Peck and Reeder, and the most recent values of constants from CODATA [48,49].

The results of the fit are shown in Fig. 3 and summarized in Table II. Two sources contribute to the uncertainties on the wavelengths: The calibration uncertainty, given by the $1\text{-}\sigma$ confidence band of the calibration function, and the uncertainty from the Zeeman model fit. The values for the wavelengths of the lines were thus determined at the sub-ppm level, which for Doppler-shift analysis of velocities corresponds to an uncertainty as low as 0.08 km s^{-1} as shown in Fig. 4. To cross-check the Zeeman model, the data were also fitted by an appropriate number of independent Gaussians, also shown in Fig. 3. The weighted average of the individual peak positions was compared to the results from the Zeeman fit and found to be in agreement within the uncertainty. This ensured that certain conditions of the Zeeman model such as the common linewidth and relative intensities predicted by the Clebsch-Gordan coefficients had no adverse effect on the central wavelength determination. Furthermore, the validity of producing the final spectrum from many 30 min acquisitions was tested by determining the peak positions in each individual acquisition. Here no suspicious trends or outliers

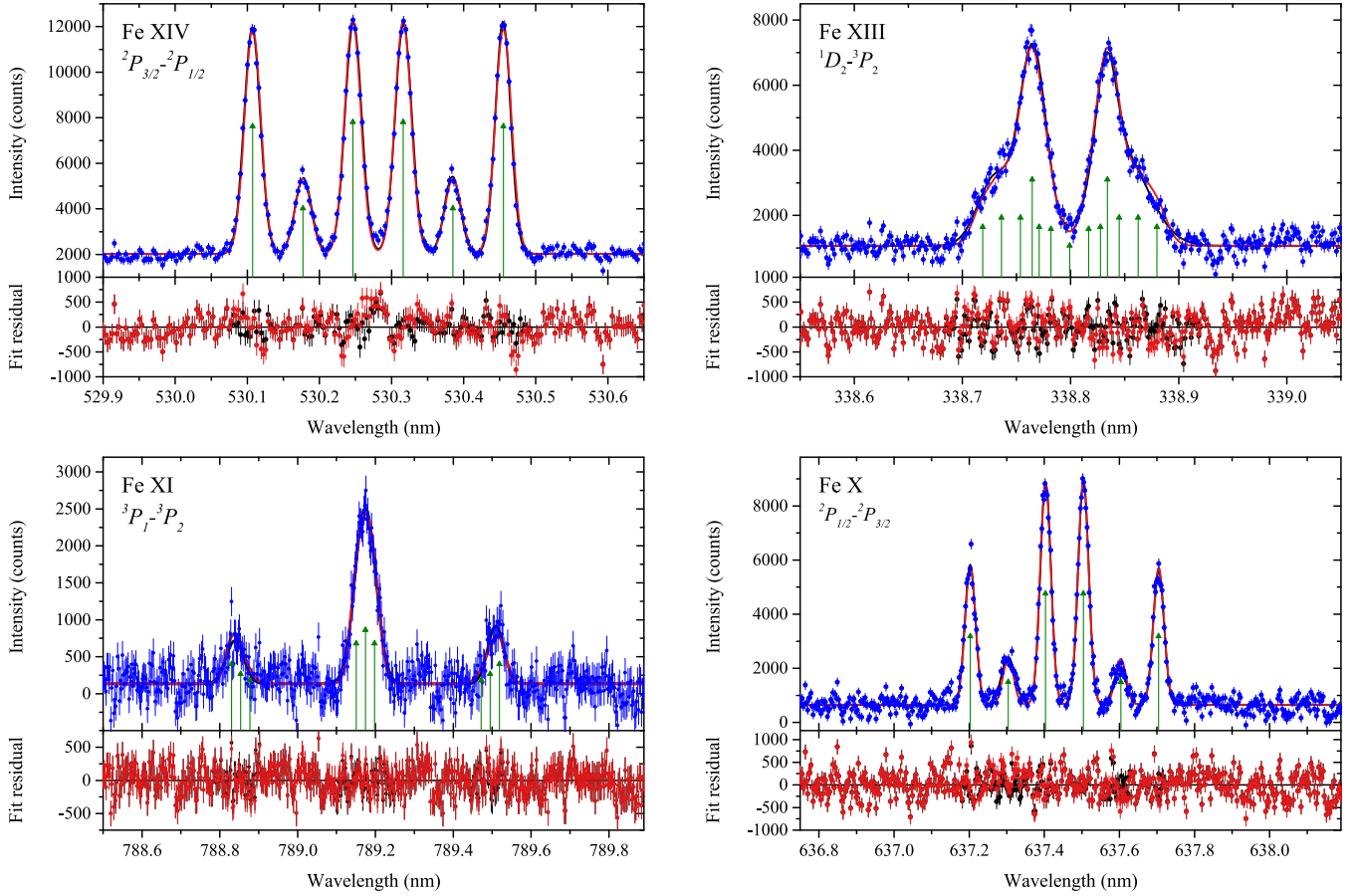


FIG. 3. Precision spectra of the Fe lines (blue circles). The Zeeman model fit and residuals are shown in red, together with its $\Delta m_J = 0, \pm 1$ components (green triangles). The fit with several independent Gaussians is shown in black. Due to its close agreement with the red line, differences between the fits are best seen in the residuals.

were found and the weighted average was in agreement with the values in Table II.

As is shown in Fig. 4, this work more than doubles the amount of laboratory (i.e., rest-frame) wavelengths of optical coronal iron lines reported on in literature [20,21,24,31,33,37,50–53]. Moreover, it shows that even very recent theoretical predictions from advanced multiconfiguration Dirac-Hartree-Fock calculations with inclusion of Breit interactions and QED corrections cannot accurately reproduce the experimental results [53]. Compared to less precise laboratory results [31], our result for the wavelength of the red coronal line at 637 nm is in perfect agreement. Previous results for the green coronal line at 530 nm, obtained by laser spectroscopy at FLASH-EBIT, deviate by 2.6σ from our result [24]. In both measurements, the calibration was

based on well-known lines of neon. However, in the laser spectroscopy work the *observed* values as found in the NIST database were considered, whereas we take the *Ritz* values, which are claimed to be more accurate but shift our calibration up by 0.1 pm in this case. Moreover, in the laser spectroscopy work, six neon calibration lines were considered, of which only one has a shorter wavelength than the iron line. This is in contrast to the ten lines with a more balanced distribution around the Fe^{13+} line used in this work (cf. Fig. 2). Finally, in the laser spectroscopy data, an additional three calibration lines were not considered. Our investigation of this old data shows that inclusion of these can shift the calibration by as much as 0.5 pm. In order to test our results against such inconsistencies, we systematically recalibrated our spectra with a subset of reference lines; no suspicious shifts were found.

TABLE II. Overview of the main results from the Zeeman fits in Fig. 3. Refer to the main text for an explanation of the uncertainties on the wavelengths in air λ . Uncertainties on the g_J factors are purely from the fit.

Ion	Transition	λ (nm)	g	g'	T (eV/k _B)
Fe XIV	[Ne]3s ² 3p(² P _{3/2} – ² P _{1/2})	530.28113(13)	1.323(2)	0.658(3)	17.4(4)
Fe XIII	[Ne]3s ² 3p(¹ D ₂ – ³ P ₂)	338.7993(2)	1.1(1)	1.5(1)	30(12)
Fe XI	[Ne]3s ² 3p(⁴ P ₁ – ³ P ₂)	789.1742(7)	1.28(2)	1.38(9)	19(3)
Fe X	[Ne]3s ² 3p(⁵ P _{1/2} – ² P _{3/2})	637.4538(5)	0.656(4)	1.320(2)	15.9(7)

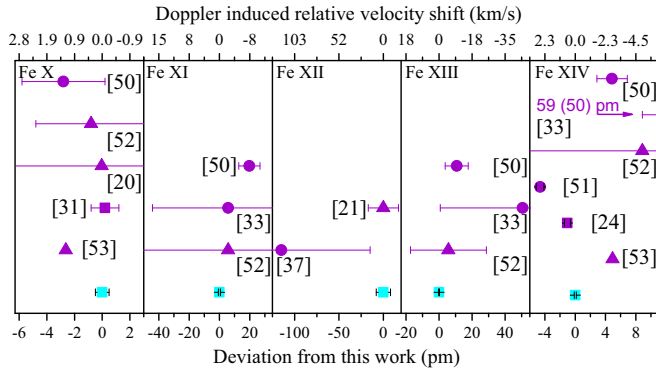


FIG. 4. Comparison between wavelengths presented in this work (cyan) and selected literature values (purple). Laboratory measurements are represented by squares, coronal ones by circles, and theory predictions by triangles. The top axis shows the magnitude of relative velocities when deviations from this work are interpreted as Doppler shifts.

The linewidths observed here were mainly due to Doppler broadening w_D and the apparatus response w_A , such that $w^2 = w_D^2 + w_A^2$. Because w_A is known from the calibration lines, the value of w as found with the Zeeman model fit allows us to extract a value for w_D , and thereby the temperature T of the ion sample as listed in Table II. Although slightly lower ion temperatures have been shown to be possible [24], in our case this would have led to a prohibitively low signal strength. Furthermore, for a more precise wavelength determination the quality of the calibration would also have to be improved.

Due to the excellent resolving power of the spectrometer, the individual Zeeman components of the Fe XIV and X transitions can clearly be discerned, and with the Zeeman model fit it is possible to extract values for the g_J factors in all four cases. These are found to be almost equal to those calculated with Landé's equation, small deviations at this level can be due to mixing of states and higher order relativistic effects. These values are important for particular methods to determine the magnetic field strength in the solar corona such as described in [9]. Furthermore, the polarization of the emit light is an important tool to determine the orientation of magnetic field lines. For the here studied magnetic dipole (M1) transitions observed perpendicular to the magnetic field

TABLE III. Comparison between measured intensity ratios of the Zeeman components $a_0/2a_{\pm 1}$ and the expected ratios based on the efficiency of the setup for different polarizations $\eta_{\text{para}}/\eta_{\text{perp}}$.

Ion	$a_0/2a_{\pm 1}$	$\eta_{\text{para}}/\eta_{\text{perp}}$
Fe XIV	0.78(1)	0.80(1)
Fe XIII	0.88(10)	1.15(1)
Fe XI	2.1(3)	2.03(1)
Fe X	1.22(3)	1.18(1)

axis, light from $\Delta m_J = 0$ components is polarized perpendicular to it and those with $\Delta m_J = \pm 1$ parallel. By taking into account the efficiencies η_{perp} and η_{para} of the grating and imaging system for the two directions of polarized light, and also accounting for the angular intensity distribution of dipole radiation, it can be shown that $a_0/2a_{\pm 1} = \eta_{\text{para}}/\eta_{\text{perp}}$. We determined the ratio of efficiencies by measuring the transfer efficiency from a polarized light source for the two polarization directions, results are compared in Table III. Note that the efficiencies strongly depend on the wavelength of the light. The results are in good agreement with each other except for the Fe XIII line. The alignment of the polarized light source might have been worse than estimated. Furthermore, for this line the Zeeman components are least well resolved and thus the uncertainty on $a_0/2a_{\pm 1}$ is rather large.

In conclusion, we provide a consistent set of rest-frame wavelengths of transitions in several highly charged iron ions which are found in the solar corona and other objects of astrophysical interest. The hitherto only inferred Fe XII line at 290.385(8) nm was observed and the strongest optical lines of four other iron charge states were measured at sub-ppm precision and the g_J factors of the involved states were extracted. This is valuable input for studies of the coronal heating problem and other astrophysical phenomena, especially considering the progressively improving spectral and spatial resolving power of astronomical observations. This data are also highly relevant for benchmarking advanced atomic theory and as stepping stone towards optical clocks based on HCIs.

This work is part of and supported by the Deutsche Forschungsgemeinschaft (DFG) Collaborative Research Centre "SFB 1225 (ISOQUANT)" and Heidelberg University.

[1] C. A. Young, *The Sun and the Phenomena of its Atmosphere* (C.C. Chatfield & Co., New Haven, 1872), pp. 153–207.
[2] W. Grotian, *Naturwissenschaften* **27**, 214 (1939).
[3] B. Edlén, *Z. Astrophys.* **22**, 30 (1943).
[4] H. Alfvén, *Arkiv Matematik, Astron. Fys.* **27a**, 1 (1941).
[5] S. R. Habbal, M. Druckmüller, H. Morgan, A. Daw, J. Johnson, A. Ding, M. Arndt, R. Esser, V. Rušin, and I. Scholl, *Astrophys. J.* **708**, 1650 (2010).
[6] S. R. Habbal, M. Druckmüller, H. Morgan, I. Scholl, V. Rušin, A. Daw, J. Johnson, and M. Arndt, *Astrophys. J.* **719**, 1362 (2010).

[7] M. Mierla, R. Schwenn, L. Teriaca, G. Stenborg, and B. Podlipnik, *Astron. Astrophys.* **480**, 509 (2008).
[8] J. T. Schmelz, D. V. Reames, R. von Steiger, and S. Basu, *Astrophys. J.* **755**, 33 (2012).
[9] H. Lin, J. R. Kuhn, and R. Coulter, *Astrophys. J. Lett.* **613**, L177 (2004).
[10] H. Li, E. L. Degl'Innocenti, and Z. Qu, *Astrophys. J.* **838**, 69 (2017).
[11] A. Ding and S. R. Habbal, *Astrophys. J. Lett.* **842**, L7 (2017).
[12] S. R. Habbal, A. Ding, M. Druckmüller, and Solar Wind Sherpas, *American Astronomical Society Meeting Abstracts* **231**, 220.07 (2018).

- [13] H. Tian, Z. Qu, Y. Chen, L. Deng, Z. Huang, H. Li, Y. Zhong, Y. Liang, J. Zhang, Y. Zhang *et al.*, *Earth Planet. Phys.* **1**, 68 (2017).
- [14] J. Schmitt and R. Wichmann, *Nature (London)* **412**, 508 (2001).
- [15] B. Fuhrmeister, J. Schmitt, and R. Wichmann, *Astron. Astrophys.* **417**, 701 (2004).
- [16] M. Rose, C. N. Tadhunter, J. Holt, C. Ramos Almeida, and S. P. Littlefair, *Mon. Not. R. Astron. Soc.* **414**, 3360 (2011).
- [17] S. Komossa, H. Zhou, T. Wang, M. Ajello, J. Ge, J. Greiner, H. Lu, M. Salvato, R. Saxton, H. Shan *et al.*, *Astrophys. J. Lett.* **678**, L13 (2008).
- [18] L. Palaversa, S. Gezari, B. Sesar, J. S. Stuart, P. Wozniak, B. Holl, and Ž. Ivezić, *Astrophys. J.* **819**, 151 (2016).
- [19] F. P. A. Vogt, I. R. Seitenzahl, M. A. Dopita, and P. Ghavamian, *Astron. Astrophys.* **602**, L4 (2017).
- [20] G. Del Zanna, K. Berrington, and H. Mason, *Astron. Astrophys.* **422**, 731 (2004).
- [21] G. Del Zanna and H. Mason, *Astron. Astrophys.* **433**, 731 (2005).
- [22] G. Del Zanna, *Astron. Astrophys.* **514**, A41 (2010).
- [23] A. A. El-Maaref, M. Ahmad, and S. Allam, *At. Data Nucl. Data Tables* **100**, 781 (2014).
- [24] K. Schnorr, V. Mäckel, N. Oreshkina, S. Augustin, F. Brunner, Z. Harman, C. H. Keitel, J. Ullrich, and J. R. Crespo López-Urrutia, *Astrophys. J.* **776**, 121 (2013).
- [25] J. C. Berengut, V. A. Dzuba, and V. V. Flambaum, *Phys. Rev. Lett.* **105**, 120801 (2010).
- [26] A. Derevianko, V. A. Dzuba, and V. V. Flambaum, *Phys. Rev. Lett.* **109**, 180801 (2012).
- [27] M. S. Safronova, V. A. Dzuba, V. V. Flambaum, U. I. Safronova, S. G. Porsev, and M. G. Kozlov, *Phys. Rev. Lett.* **113**, 030801 (2014).
- [28] M. G. Kozlov, M. S. Safronova, J. R. C. López-Urrutia, and P. O. Schmidt, *Rev. Mod. Phys.* **90**, 045005 (2018).
- [29] A. Windberger, J. R. Crespo López-Urrutia, H. Bekker, N. S. Oreshkina, J. C. Berengut, V. Bock, A. Borschevsky, V. A. Dzuba, E. Eliav, Z. Harman, U. Kaldor, S. Kaul, U. I. Safronova, V. V. Flambaum, C. H. Keitel, P. O. Schmidt, J. Ullrich, and O. O. Versolato, *Phys. Rev. Lett.* **114**, 150801 (2015).
- [30] S. Murata, T. Nakajima, M. S. Safronova, U. I. Safronova, and N. Nakamura, *Phys. Rev. A* **96**, 062506 (2017).
- [31] G. Brenner, J. R. Crespo López-Urrutia, S. Bernitt, D. Fischer, R. Ginzler, K. Kubiček, V. Mäckel, P. H. Mokler, M. C. Simon, and J. Ullrich, *Astrophys. J.* **703**, 68 (2009).
- [32] G. D. Sandlin, G. E. Brueckner, and R. Tousey, *Astrophys. J.* **214**, 898 (1977).
- [33] J. T. Jefferies, F. Q. Orrall, and J. B. Zirker, *Sol. Phys.* **16**, 103 (1971).
- [34] J. R. Crespo López-Urrutia, A. Dorn, R. Moshhammer, and J. Ullrich, *Phys. Scr.* **1999**, 502 (1999).
- [35] S. W. Epp, J. R. Crespo López-Urrutia, M. C. Simon, T. Baumann, G. Brenner, R. Ginzler, N. Guerassimova, V. Mäckel, P. H. Mokler, B. L. Schmitt, H. Tawara, and J. Ullrich, *J. Phys. B: At., Mol. Opt. Phys.* **43**, 194008 (2010).
- [36] K.-N. Huang, *At. Data Nucl. Data Tables* **30**, 313 (1984).
- [37] A. Kramida, Yu. Ralchenko, J. Reader, and NIST ASD Team, *NIST Atomic Spectra Database* (ver. 5.5.1), [Online]. Available: <https://physics.nist.gov/asd> [2018, January 5]. National Institute of Standards and Technology, Gaithersburg, MD (2017).
- [38] See Supplemental Material at <http://link.aps.org/supplemental/10.1103/PhysRevA.98.062514> for compendium of the employed equations, constants, and reference wavelengths.
- [39] K. Burns, K. B. Adams, and J. Longwell, *J. Opt. Soc. Am.* **40**, 339 (1950).
- [40] J. C. Ehrhardt, Analysis of the atomic spectrum of gold, Ph.D. thesis, University of California, Berkeley, 1970.
- [41] W. F. Meggers and C. J. Humphreys, *J. Res. Natl. Bur. Stand. USA* **13**, 293 (1934).
- [42] W. F. Meggers, C. H. Corliss, and B. F. Scribner, *Natl. Bur. Stand. (U.S.)* **145**, 403 (1975).
- [43] B. A. Palmer and R. Engleman, *Los Alamos National Laboratory Report LA-9615* (1983).
- [44] R. Engleman, U. Litzén, H. Lundberg, and J.-F. Wyart, *Phys. Scr.* **57**, 345 (1998).
- [45] W. Whaling, W. Anderson, M. Carle, J. Brault, and H. Zarem, *J. Quant. Spectrosc. Radiat. Transfer* **53**, 1 (1995).
- [46] G. Norlén, *Phys. Scr.* **8**, 249 (1973).
- [47] M. F. Gu, *Can. J. Phys.* **86**, 675 (2008).
- [48] E. R. Peck and K. Reeder, *J. Opt. Soc. A* **62**, 958 (1972).
- [49] P. J. Mohr, D. B. Newell, and B. N. Taylor, *Rev. Mod. Phys.* **88**, 035009 (2016).
- [50] M. B. Lyot, *Mon. Not. R. Astron. Soc.* **99**, 580 (1939).
- [51] M. Rybanský, V. Rušin, V. Dermendjiev, and G. Buyukliyev, *Contrib. Astron. Obs. Skalnaté Pleso* **15**, 419 (1986).
- [52] V. Kaufman and J. Sugar, *J. Phys. Chem. Ref. Data* **15**, 321 (1986).
- [53] M. Bilal, A. V. Volotka, R. Beerwerth, and S. Fritzsche, *Phys. Rev. A* **97**, 052506 (2018).